Supporting information:

Y. Guo, C.L. Partch, J. Key, P.B. Card, V. Pashkov, A. Patel, R.K. Bruick, H. Wurdak, and K.H. Gardner – "Regulating the ARNT/TACC3 axis: Multiple approaches to manipulating protein/protein interactions with small molecules"

Supporting Methods

Cell culture and transfection

HEK293T and HeLa cells were maintained in Dulbecco's modified Eagle's medium (Thermo Scientific) supplemented with 10% fetal bovine serum, 2 mM L-glutamine, 100 U/ml penicillin and 100 µg/ml streptomycin. Human hepatocellular carcinoma Hep3B cells were grown in DMEM/high glucose media (HyClone, # SH30022.01) supplemented with 10% of fetal bovine serum (Atlanta Biologicals), 20 mM HEPES buffer (pH 7.4), 1 mM sodium pyruvate, 100 U/ml penicillin and 100 µg/ml streptomycin (Invitrogen). Hep3B cells at ~80% confluence were incubated with compound for 2 hr prior to incubation under normoxic (~20% O_2) or hypoxic (1% O_2) conditions using a hypoxic incubator (COY Laboratory Products Inc.). Plasmids were transfected using Lipofectamine 2000 (Invitrogen). Cells were harvested in IP lysis buffer (50 mM Tris pH 7.5, 150 mM NaCl, 0.5% (v/v) NP-40 and freshly added EDTA-free protease inhibitors (Roche)). Cell lysates were clarified by centrifugation for 10 min at 21,000 g at 4°C and used for immunoprecipitation or Western blot.

Protein expression and purification

Proteins were expressed in BL21(DE3) cells (New England Biolabs), grown in LB or M9 minimal media (with 1 g/L $^{15}NH_4Cl$ or 3 g/L U-^{13}C glucose for isotope labeling) at 37°C and induced with 500 µM IPTG at an OD_{600} of 0.70. After overnight growth at 20°C, cells were harvested by centrifuging at 4°C, 4600 g for 40 min. Pellets were resuspended in buffers for affinity chromatography (Ni^{2+} affinity: 50 mM Tris pH 7.5, 150 mM NaCl, 20 mM imidazole, 5 mM beta-mercaptoethanol; glutathione affinity: 1X phosphate buffered saline) and stored at -80°C. Purification was conducted using affinity chromatography (Ni Sepharose High Performance or Glutathione

Sepharose 4B, GE Healthcare). Affinity tags (GST, His or HisGβ1) were cleaved by His_6-TEV protease overnight at 4°C, followed by size-exclusion chromatography (Superdex 75, GE Healthcare). Samples of ARNT2 PAS-B used for triple resonance NMR experiments for backbone chemical shift assignment were kept in a buffer of 25 mM Tris (pH 7.3), 17 mM NaCl, 2.5 mM TCEP and 10% (v/v) D_2O. Other NMR experiments were done in 25 mM Tris (pH 7.5), 17 mM NaCl, 5 mM beta-mercaptoethanol and 10% (v/v) D_2O.

X-ray crystallography

Single crystals of ARNT PAS-B were grown by hanging drop vapor diffusion against 2 - 2.2 M ammonium sulfate, 3% (wt/vol) PEG 400, 2% (wt/vol) polyethyleneimine, 100 mM Tris (pH 8.5) solutions. Drops contained 5 µl of 500 µM ARNT PAS-B mixed with 5 µl of precipitant solution. Crystals were observed within minutes and reached their maximum sizes within 1 day.

Diffraction data were obtained at the Structural Biology Center at the Advanced Photon Source (Argonne National Laboratory, Argonne, IL). All data were indexed and scaled with HKL2000.(*1*) Molecular replacement was performed using phaser(*2*) using the ARNT subunit of the HIF-2α/ARNT PAS-B heterodimer as a search model (chain B of PDB 3F1P).(*3*) Refinement was completed using PHENIX and COOT(*4, 5*). Coordinates have been deposited with the RCSB database and assigned accession number 4EQ1. Cavities were identified using the program VOIDOO using a 1.2 Å radius probe.(*6*)

NMR spectroscopy

NMR experiments for backbone and sidechain chemical shift assignments of ARNT2 PAS-B were carried out at 35°C on Varian Inova 600 and 800 MHz spectrometers using a 400 µM sample of uniformly $^{15}N/^{13}C$ labeled ARNT2 PAS-B. Backbone assignments were based on data from standard 3D triple resonance experiments: HNCACB, CBCA(CO)NH, HNCO, H(CCO)HN-TOCSY and (H)C(CO)HN-TOCSY.(*7*) Sidechain chemical shift assignments were based on HCCH-TOCSY and

simultaneous ^{15}N,^{13}C-edited NOESY data. Chemical shift assignments of ARNT PAS-B were used as previously established.(*8*) All NMR data were processed with NMRpipe/NMRDraw (*9*) and analyzed with NMRviewJ (Version 8.2.29, One Moon Scientific). Backbone assignment results were uploaded to TALOS+ web server(*10*) for chemical-shift based secondary structure analysis. Heat maps of minimum chemical shift perturbations and peak broadening onto the ARNT PAS-B crystal structure and an ARNT2 PAS-B homology model (generated by SWISS-MODEL(*11*) from the ARNT PAS-B crystal structure) were generated by PyMOL (Version 1.5.0.4, Schrödinger, LLC).

Immunofluorescence

HEK293 cells were grown to 70% confluency and treated with KHS101 compound at concentrations indicated in the figures. Incubation was for 14 hr in a humidified incubator at 37 °C and 5% CO_2. Next, cells were fixed in 4% (v/v) paraformaldehyde/PBS for 15 minutes at room temperature. Cells were washed in PBS and permeabilized with a PBS-based buffer containing 0.3% Triton X-100 and 5% FBS. Incubation was for one hour at room temperature to prevent nonspecific binding of antibodies. Cells were incubated at 4°C overnight with the following primary antibodies: TACC3 AB1 (Rabbit polyclonal HPA005781, Sigma-Aldrich), TACC3 AB2 (Rabbit polyclonal 5640-1, Epitomics). After washing with PBS, cells were incubated for 40 min at room temperature with a Cy3–conjugated rabbit secondary antibody (Jackson ImmunoResearch Laboratories) and washed with PBS in the presence of DAPI (0.1 ng/mL). Fluorescent cells were visualized using a digital inverted microscope and similar exposure time (EVOS, Advanced Microscopy Group (AMG)). ImageJ quantification of TACC3 staining intensity was normalized to DAPI signal with DMSO.

qPCR primers

The following primer sets were used to amplify target genes: Cyclophilin B, forward 5'-tgccatcgccaaggagtag-3' and reverse 5'- tgcacagacggtcactcaaa-3'; HIF-2α, forward 5'-gcgacaatgacagctgacaa -3' and reverse 5'- cagcatcccgggacttct -3'; EPO, forward 5'-gaggccgagaatatcacgacggg -3' and reverse 5'- tgcccgacctccatcctcttccag -3'; GLUT1, forward 5'-

cttttctgttgggggcatgat -3' and reverse 5'- ccgcagtacacaccgatgat -3'; HIF-1α, forward 5'- tgccacatcatcaccatatagaga -3' and reverse 5'- tccttttcctgctctgtttgg -3'; PGK1, forward 5'- ttaaagggaagcgggtcgtta -3' and reverse 5'- tccattgtccaagcagaatttga -3'.

Supporting Results

Supporting Figure S1. KG-548 analogs do not disrupt ARNT PAS-B/TACC3-CT complex. **a.** Structure of KG2-006 (Maybridge). **b.** Structure of KG2-007 (Maybridge). **c.** Titration of KG2-006 into ^{15}N ARNT PAS-B (increasing ligand concentrations from light to dark purple: 0, 62.5, 125, 250, 500, 750, 1000 μM; protein concentration: 200 μM). Fast exchange behavior is observed in some of the peaks, indicating relatively weak binding affinity compared with KG-548. **d.** Titration of KG2-007 into ^{15}N ARNT PAS-B (same concentrations as panel **c**). Spectrum was not perturbed by the addition of KG2-007, indicating an even weaker binding to ARNT PAS-B. **e.** Pulldown experiment with KG-548, KG2-006 and KG2-007 (500 μM of all compounds; 5 μM ARNT, 10 μM TACC3). Neither of the KG2 compounds is able to break up the ARNT PAS-B/TACC3-CT complex. **f.** Co-immunoprecipitation experiment of KG2-006 and KG2-007 on full length ARNT/TACC3 in whole cell lysate. At concentrations up to 2 mM, neither of the KG2 compounds is able to break up the ARNT/TACC3 complex as KG-548 does, consistent with lower binding affinities of these derivatives.

Supporting Figure S2. Sequence alignment of ARNT homologs on the PAS-B domain. The PAS-B domain of ARNT shows a high degree of sequence similarity to the corresponding ARNT2 PAS-B domain. Notably, residues adjacent to the small cavities inside of ARNT PAS-B (black dots) are also chiefly conserved in ARNT2 PAS-B.

Supporting Figure S3. The PAS-B domains from ARNT and ARNT2 have similar structures and TACC3 binding surfaces. a. ^{15}N/^{1}H HSQC spectrum of ARNT2 PAS-B, with peaks corresponding to backbone amides labeled with the residue numbers identified in the backbone chemical shift assignment (35°C, pH 7.3). Peaks comparable to the far downfield peak (ca. 11.2 ppm ^{1}H, 119.5 ppm

^{15}N; assigned to residue E377) have been observed for other PAS domains; the distinctive shifts of this peak arise from the tertiary structure near the N-terminus of the Fα helix and provide a qualitative verification of a PAS domain tertiary structure. **b**. TALOS+ secondary structure analysis based on backbone chemical shifts.(*12*) Residues assigned to α–helix (red, negative) and β-sheet (blue, positive) are mapped along the amino acid sequence of ARNT PAS-B (upper) and ARNT2 PAS-B (lower), showing very similar secondary structures in both proteins. Residues in ARNT2 PAS-B indicated with white circles are unassigned, which we attribute to problems with line broadening caused by transient dimerization, as we have observed to varying degrees with several PAS domains.(*8, 13*) **c.** A SWISS-MODEL(*11*) homology model of ARNT2 PAS-B (purple) aligns well with ARNT PAS-B crystal structure (blue). Residues demonstrated to be important for TACC3 binding are also conserved in the tertiary structure (E398, K417 for ARNT PAS-B(*14*); E372, K391 for ARNT2 PAS-B). **d.** Ni-NTA pulldown experiments demonstrate that ARNT2 PAS-B interacts with TACC3-CT, and that the affinity for this interaction is lessened by point mutations to residues analogous to those involved in ARNT/TACC3 binding (Fig. S3c). **e.** ^{15}N/^{1}H HSQC spectra of ARNT2 PAS-B E372A and K391A (red), each overlaid with spectra of wildtype ARNT2 PAS-B (black). The minimal effects of the E372A and K391A mutations on the patterns of peaks in the ^{15}N/^{1}H HSQC spectra, including the location of the E377 peak reflecting PAS domain tertiary structure (Fig. S3a), strongly suggest that these changes have limited effects on the structure of this domain.

Supporting Figure S4. KG-548 binds similarly to ARNT2 PAS-B and ARNT PAS-B, and disrupts ARNT2/TACC3 interactions. **a.** ^{15}N/^{1}H HSQC spectra of 100 μM ^{15}N-labeled ARNT2 PAS-B titrated with increasing concentrations of KG-548 (from none (light purple) to 100 μM (dark purple)). We observed slow exchange behavior, analogous to the ARNT/KG-548 titration (Fig. 3a). **b.** Minimum chemical shift perturbation analysis(*15*) of KG-548 effects on ARNT2 PAS-B, showing similar patterns of shifts as observed with ARNT PAS-B (Fig. 3b). **c.** Side-by-side comparison of ARNT PAS-B structure (including internal cavities) and chemical shift perturbation data mapped onto a homology model of ARNT2 PAS-B (scale as indicated). Most of the affected residues are close to the location of

the cavity inside of ARNT PAS-B. **d.** Binding of KG-548 can disrupt ARNT2 PAS-B/TACC3-CT interaction by pulldown assay.

Supporting Figure S5. KG-548 binds to different bHLH/PAS PAS-B domains with differential affinities. a. $^{15}N/^{1}H$ HSQC spectra of 100 μM ^{15}N-labeled ARNT PAS-B in the absence and presence of 100 μM KG-548. A large number of residues are affected by compound addition, with correspondingly large chemical shift changes, consistent with KG-548 binding to ARNT. **b.** Superposition of $^{15}N/^{1}H$ HSQC spectra of 100 μM ^{15}N-labeled BMAL1 PAS domain titrated with 100 μM KG-548. Very limited chemical shift changes were observed, suggesting that there is effectively less interaction between protein and ligand at these concentrations. **c.** Superposition of $^{15}N/^{1}H$ HSQC spectra of 100 μM ^{15}N-labeled HIF-2α PAS-B titrated with 100 μM KG-548. No chemical shift changes were observed, suggesting that there is effectively no interaction between protein and ligand at these concentrations.

Supporting Figure S6. Validation of ARNT PAS-B/TACC3-CT AlphaScreen protein/protein interaction assay. a. Schematic of the AlphaScreen protein/protein interaction assay used to estimate the affinity of the ARNT/TACC3-CT complex. GST and His_6-tagged proteins will recruit donor and acceptor AlphaScreen beads into close enough proximity that a luminescence signal will be detected. **b.** Titration of either untagged ARNT PAS-B (red, right y-axis) or TACC3 (blue, left y-axis) into a preformed ARNT/TACC3-CT complex competes with the corresponding proteins in complex, decreasing the AlphaScreen luminescence signal. Dose-dependence curves generated from these titrations suggest that each protein has a 2-3 μM IC_{50} for complex disruption.

Supporting Figure S7. KHS101 does not directly regulate the formation of a minimal ARNT/TACC3 complex. a. Structure of KHS101.(*16*) **b.** At concentrations up to 250 μM, KHS101 fails to disrupt the complex of minimal His-ARNT PAS-B and GST-TACC3-CT fragments by *in vitro* pulldown assays. **c.** KHS101 is unable to interfere with *in vitro* interactions between ARNT2 PAS-

B/TACC3-CT. In contrast to KG-548, addition of KHS101 (up to concentrations of 50 μM) into an *in vitro* Ni-NTA pulldown assay shows no significant effect on the stability of a complex between ARNT2 PAS-B and TACC3-CT. **d.** $^{15}N/^{1}H$ HSQC spectra of 100 μM ^{15}N ARNT PAS-B in the absence (black) or presence (red) of 100 μM KHS101 show no ligand-induced effects, indicating no direct binding of KHS101 to ARNT PAS-B. **e.** $^{15}N/^{1}H$ HSQC spectra of 100 μM GCN4-TACC3-min (610-631) dimer titrated with 100 μM KHS101 (apo: black, holo: red)). No significant peak perturbation is observed, indicating no direct binding of KHS101 to the TACC3-CT.

Supporting Figure S8. Specificity of KHS101 effects on TACC3 levels. a. Blot of ARNT and β-actin protein levels in HEK293T cells after 5 μM KHS101 treatment as described before. ARNT level was not changed in the presence of KHS101, indicating its effect in protein turnover is specific to TACC3. **b.** Quantification of data presented in Fig. S8a, showing no effect of KHS101 on the ARNT turnover rate. **c.** Blot of TACC3 and β-actin protein levels in HEK293T cells after treatment with either DMSO or 100 μM KG-548 in the presence of 100 μg/ml cycloheximide. **d.** Quantification of data presented in Fig. S8c (DMSO, KG-548 treatments) or Fig. 5a (KHS101 treatment) demonstrates that turnover effects are specific to KHS101. **e.** Structure of KHS91, an inactive analog of KHS101.(*16*) **f.** Blot of TACC3 and β-actin protein levels in HEK293T cells after treatment with either DMSO or 5 μM KHS91 in the presence of 100 μg/ml cycloheximide. **g.** Quantification of data presented in Fig. S8e, showing no effect of KHS91 on the TACC3 turnover rate.

Supporting Figure S9. TACC3 level is reduced by KHS101 in a dose-dependent manner

a. HEK293T cells were treated with KHS101 (0, 2, 6, and15 μM) and immunostained with TACC3 AB2 after 14 hr. TACC3 intensity was negatively affected by KHS101, consistent with results shown in Fig. 5c using the independent TACC3 AB1. **b.** Quantification of TACC3 intensity as determined by the anti-TACC3 immunostaining shown in Fig. 5c (AB1) and Fig. S9a (AB2). Overall TACC3 staining intensity levels were reduced to approximately 90% after KHS101 treatment measured by two different TACC3 antibodies. **c.** HEK293T cells were treated with KHS101 (0-25 μM) and harvested after 16 hr.

Quantification of TACC3 levels by immunoblots in the lysates of these cells show a dose-dependent reduction in TACC3 levels with an approximate IC_{50} of 3 μM and final reduction to approximately the same 90% level as seen in cells (Fig. S9b).

Supporting Table S1: Listing of compounds in fragment library used for NMR-based screening of ARNT PAS-B. For each compound, information listed includes chemical structure, compound name, unique identifier for database, CAS number, supplier, formula and molecular weight. Table provided separately as a Microsoft Excel file.

Supporting References

1. Otwinowski, Z., and Minor, W. (1997) Processing of X-ray diffraction data collected in oscillation mode, *Meth. Enz. 276*, 307-326.
2. McCoy, A. J., Grosse-Kunstleve, R. W., Adams, P. D., Winn, M. D., Storoni, L. C., and Read, R. J. (2007) Phaser crystallographic software, *J. Appl. Crystallogr. 40*, 658-674.
3. Scheuermann, T. H., Tomchick, D. R., Machius, M., Guo, Y., Bruick, R. K., and Gardner, K. H. (2009) Artificial ligand binding within the HIF2alpha PAS-B domain of the HIF2 transcription factor, *Proc Natl Acad Sci U S A 106*, 450-455.
4. Emsley, P., and Cowtan, K. (2004) Coot: model-building tools for molecular graphics, *Acta Crystallogr D Biol Crystallogr 60*, 2126-2132.
5. Adams, P. D., Afonine, P. V., Bunkoczi, G., Chen, V. B., Davis, I. W., Echols, N., Headd, J. J., Hung, L. W., Kapral, G. J., Grosse-Kunstleve, R. W., McCoy, A. J., Moriarty, N. W., Oeffner, R., Read, R. J., Richardson, D. C., Richardson, J. S., Terwilliger, T. C., and Zwart, P. H. (2010) PHENIX: a comprehensive Python-based system for macromolecular structure solution, *Acta Crystallogr D Biol Crystallogr 66*, 213-221.
6. Kleywegt, G. J., and Jones, T. A. (1994) Detection, delineation, measurement and display of cavities in macromolecular structures, *Acta Crystallogr D Biol Crystallogr 50*, 178-185.
7. Sattler, M., Schleucher, J., and Griesinger, C. (1999) Heteronuclear multidimensional NMR experiments for the structure determination of proteins in solution employing pulsed field gradients, *Prog. Nucl. Magn. Reson. Spectrosc. 34*, 93-158.
8. Card, P. B., Erbel, P. J. A., and Gardner, K. H. (2005) Structural basis of ARNT PAS-B dimerization: Use of a common beta-sheet interface for hetero- and homodimerization, *J. Mol. Biol. 353*, 664-677.
9. Delaglio, F., Grzesiek, S., Vuister, G. W., Zhu, G., Pfeifer, J., and Bax, A. (1995) NMRPipe: a multidimensional spectral processing system based on UNIX pipes, *J. Biomol. NMR 6*, 277-293.
10. Shen, Y., Delaglio, F., Cornilescu, G., and Bax, A. (2009) TALOS+: a hybrid method for predicting protein backbone torsion angles from NMR chemical shifts, *J. Biomol. NMR 44*, 213-223.
11. Arnold, K., Bordoli, L., Kopp, J., and Schwede, T. (2006) The SWISS-MODEL workspace: a web-based environment for protein structure homology modelling, *Bioinformatics 22*, 195-201.
12. Shen, Y., Delaglio, F., Cornilescu, G., and Bax, A. (2009) TALOS+: a hybrid method for predicting protein backbone torsion angles from NMR chemical shifts, *Journal of biomolecular NMR 44*, 213-223.
13. Lee, J., Tomchick, D. R., Brautigam, C. A., Machius, M., Kort, R., Hellingwerf, K. J., and Gardner, K. H. (2008) Changes at the KinA PAS-A dimerization interface influence histidine kinase function, *Biochemistry 47*, 4051-4064.
14. Partch, C. L., and Gardner, K. H. (2011) Coactivators necessary for transcriptional output of the hypoxia inducible factor, HIF, are directly recruited by ARNT PAS-B, *Proc Natl Acad Sci U S A 108*, 7739-7744.
15. Farmer, B. T., Constantine, K. L., Goldfarb, V., Friedrichs, M. S., Wittekind, M. G., Yanchunas, J. J., Robertson, J. G., and Mueller, L. (1996) Localizing the $NADP^+$ binding site on the MurB enzyme by NMR, *Nat. Struct. Biol. 3*, 995-997.
16. Wurdak, H., Zhu, S., Min, K. H., Aimone, L., Lairson, L. L., Watson, J., Chopiuk, G., Demas, J., Charette, B., Halder, R., Weerapana, E., Cravatt, B. F., Cline, H. T., Peters, E. C., Zhang, J., Walker, J. R., Wu, C., Chang, J., Tuntland, T., Cho, C. Y., and Schultz, P. G. (2010) A small molecule accelerates neuronal differentiation in the adult rat, *Proc Natl Acad Sci U S A 107*, 16542-16547.

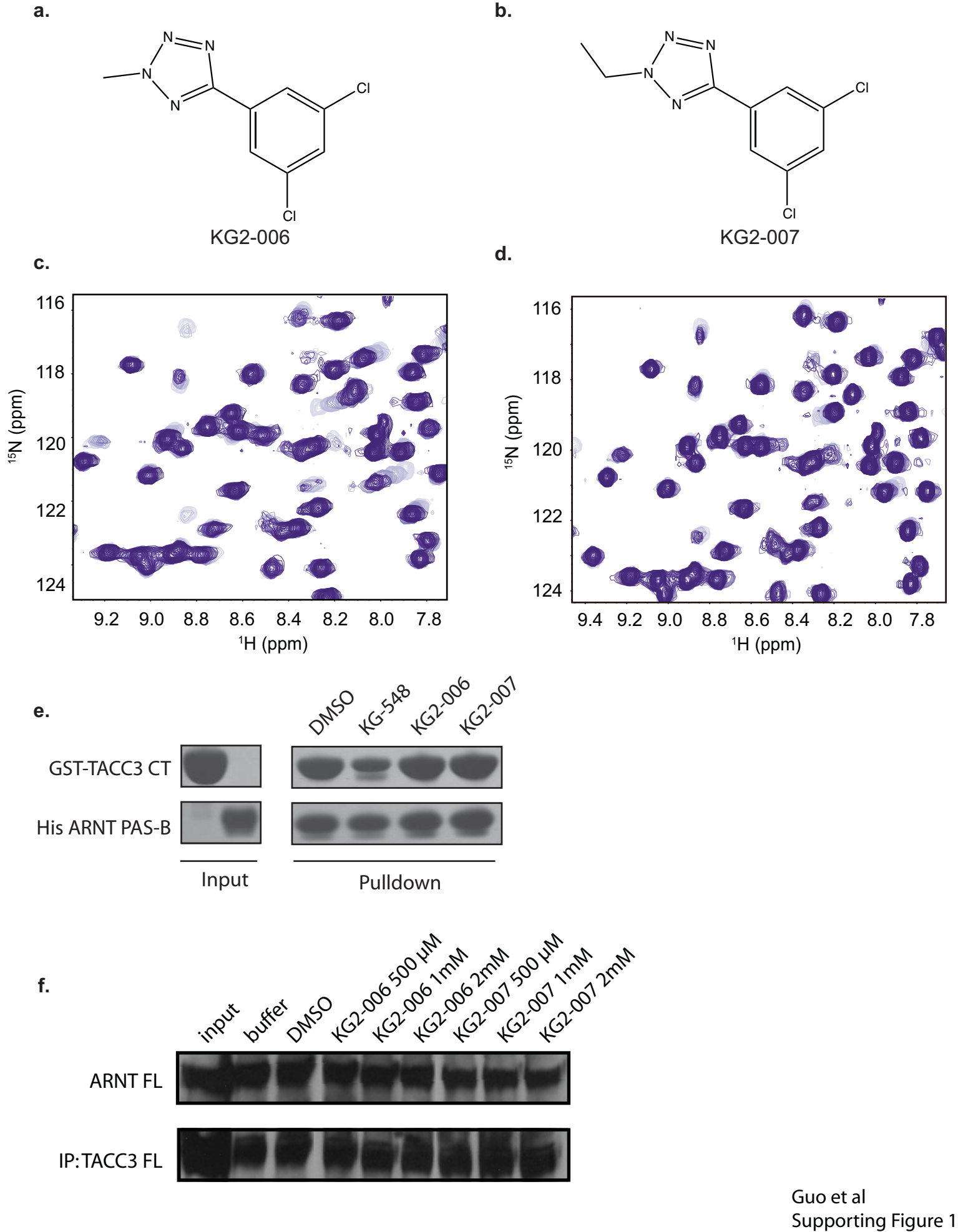

Guo et al
Supporting Figure 1

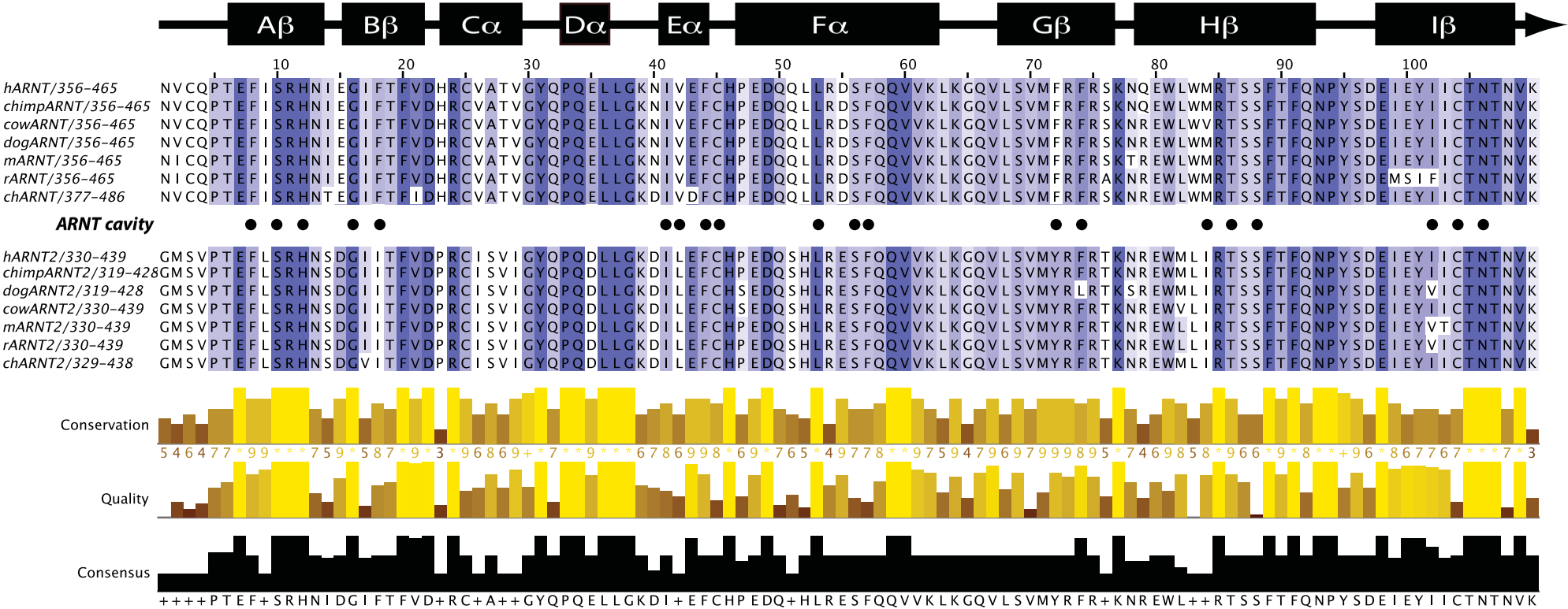

Guo et al
Supporting Figure 2

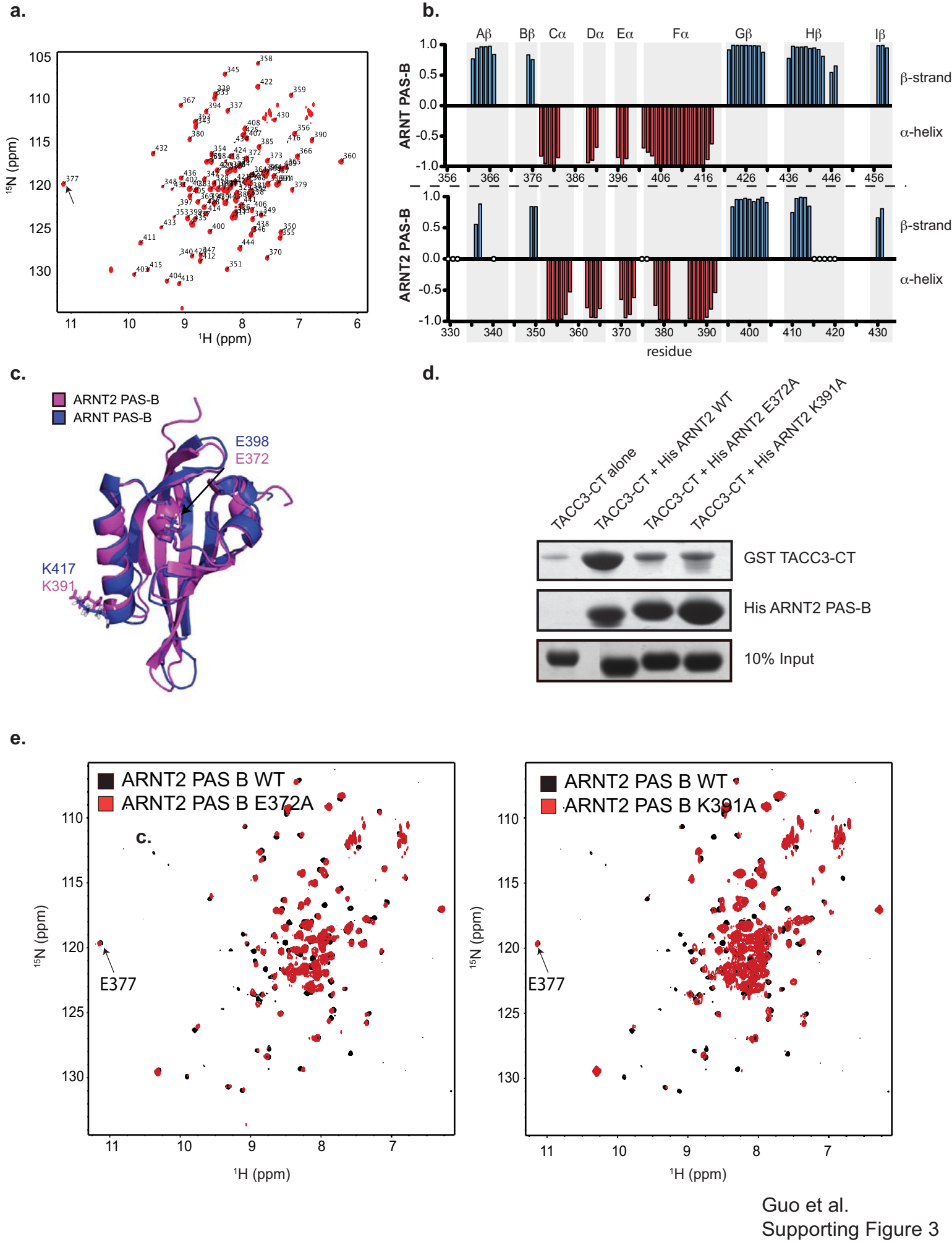

Guo et al.
Supporting Figure 3

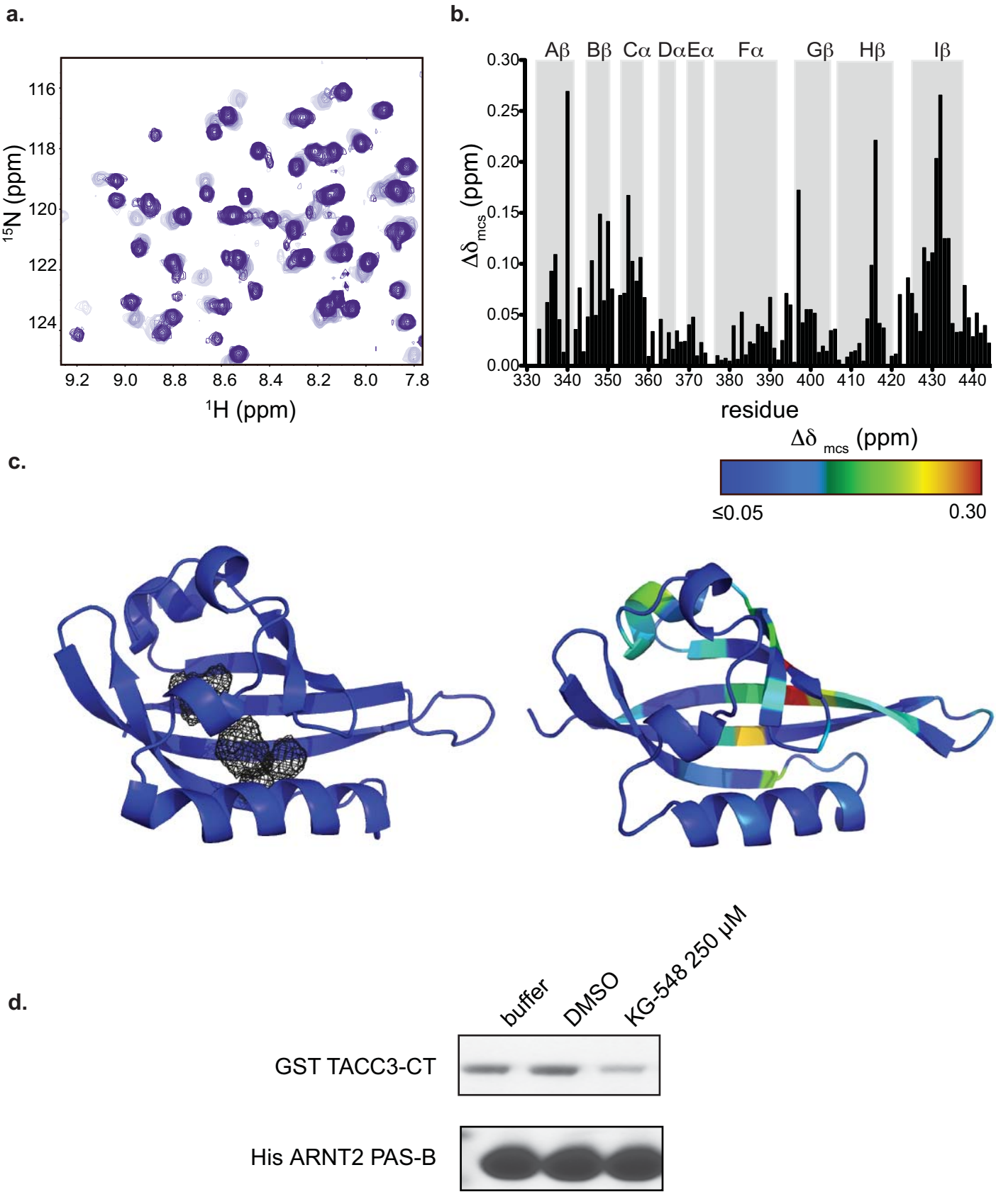

Guo et al.
Supporting Figure 4

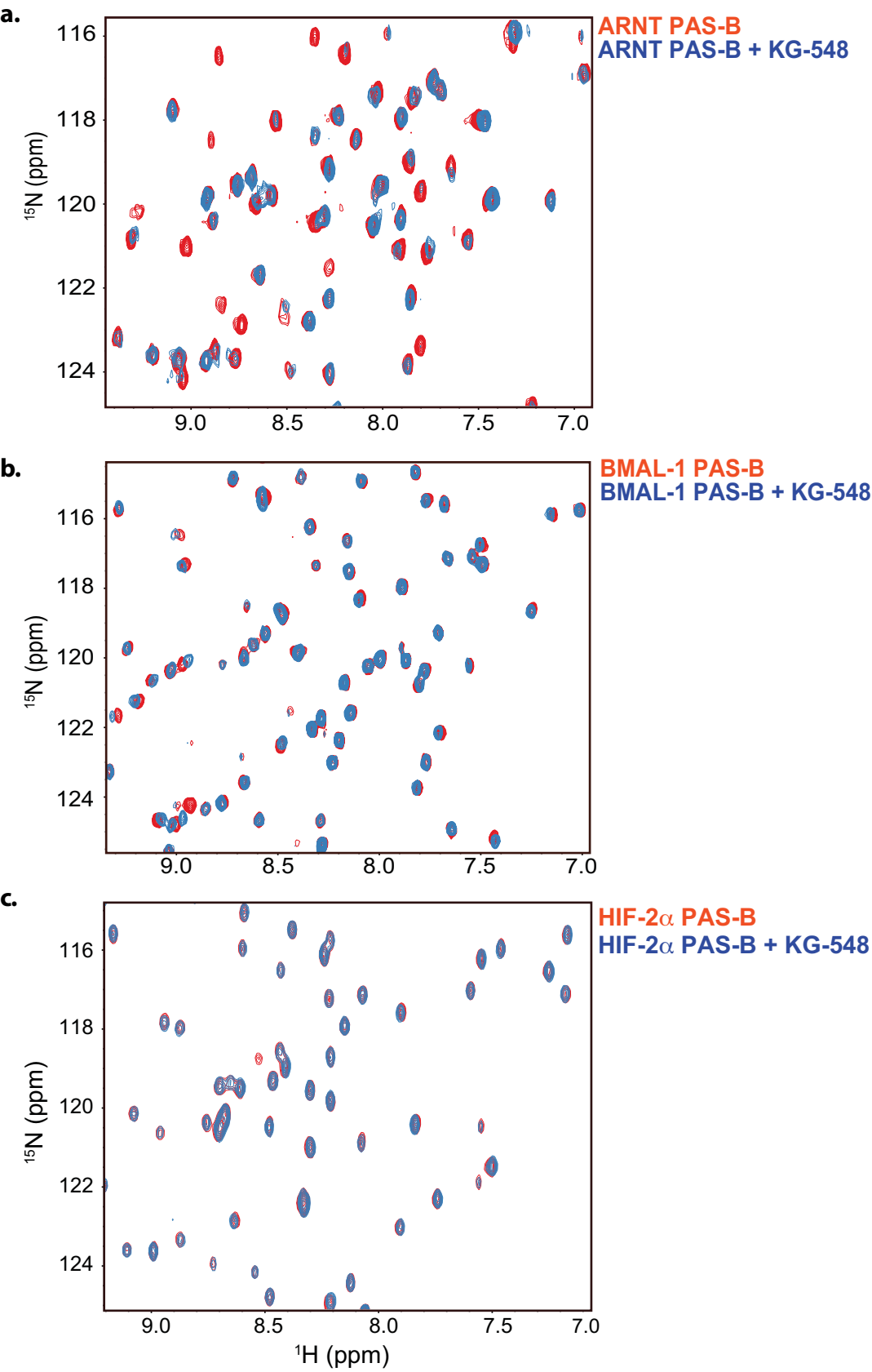

Guo et al
Supporting Figure 5

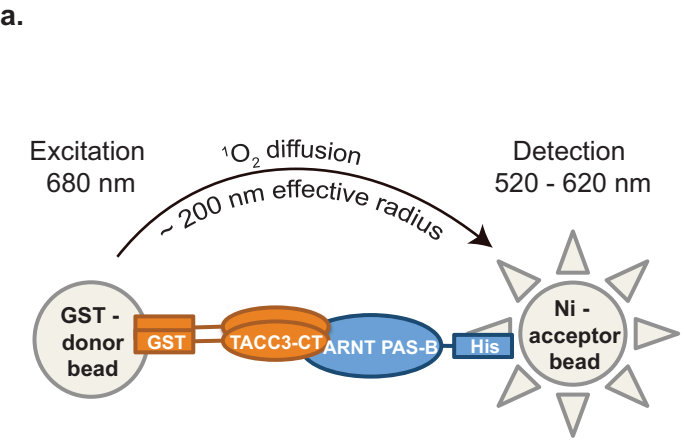

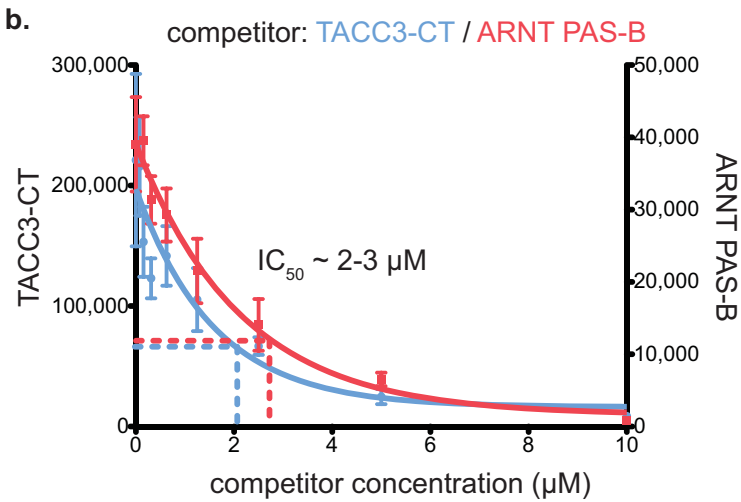

Guo et al.
Supporting Figure 6

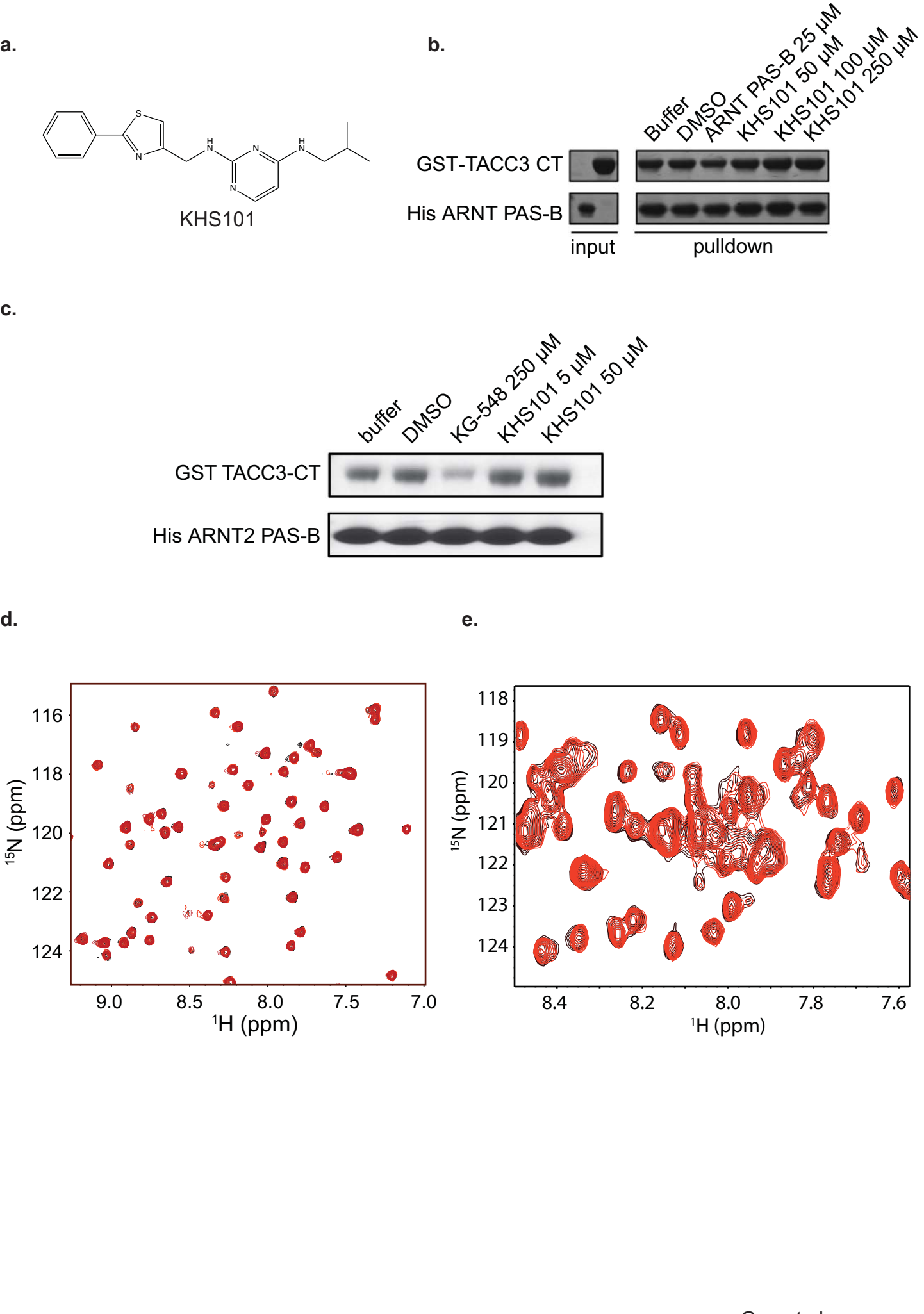

Guo et al
Supporting Figure 7

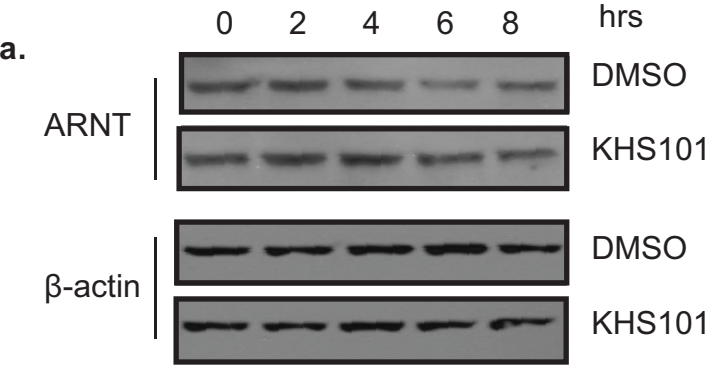

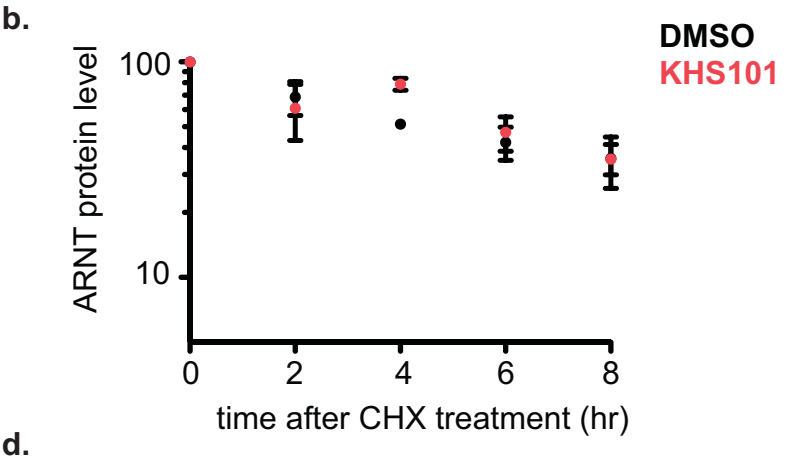

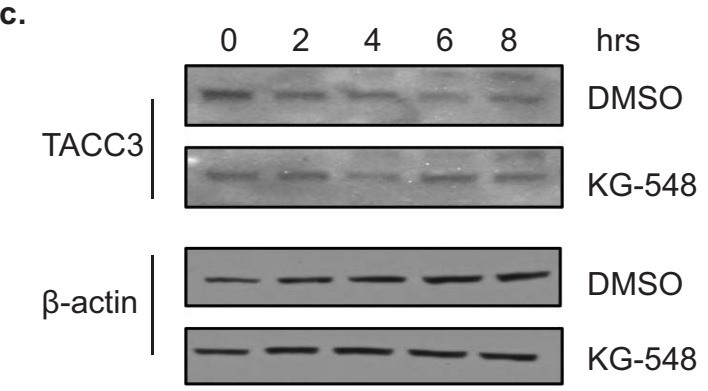

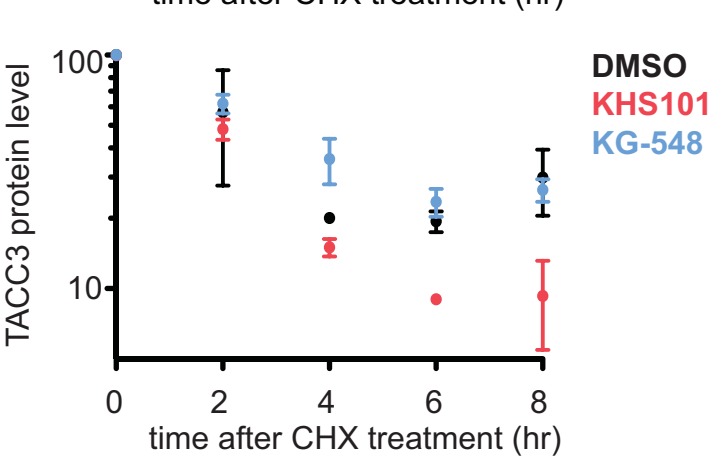

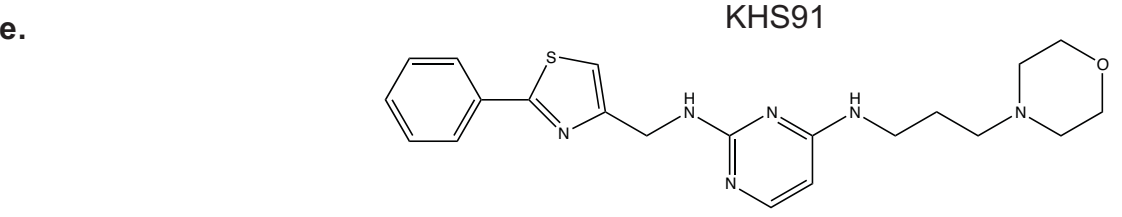

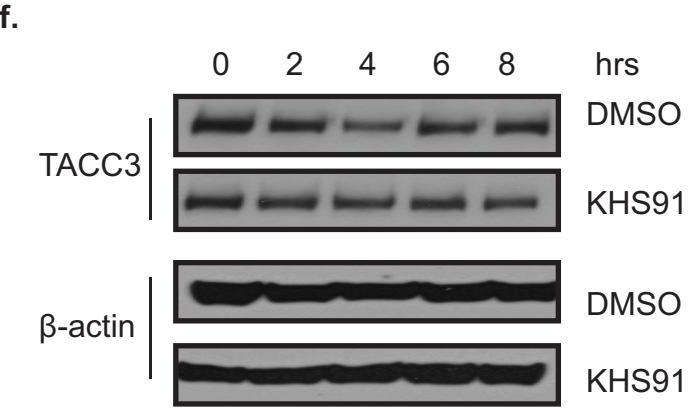

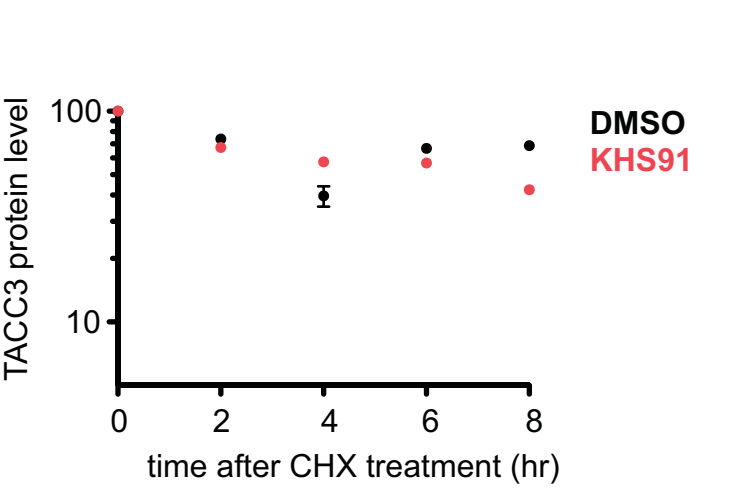

Guo et al
Supporting Figure 8

a.

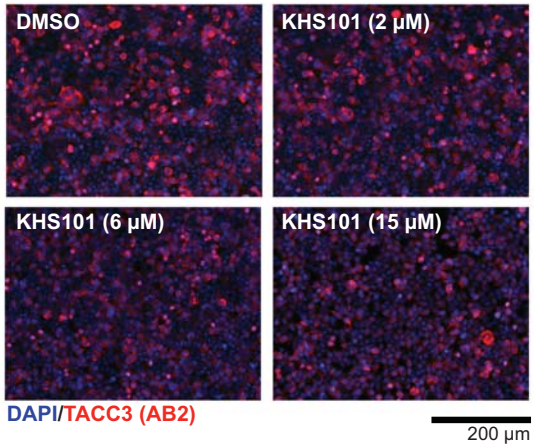

b.

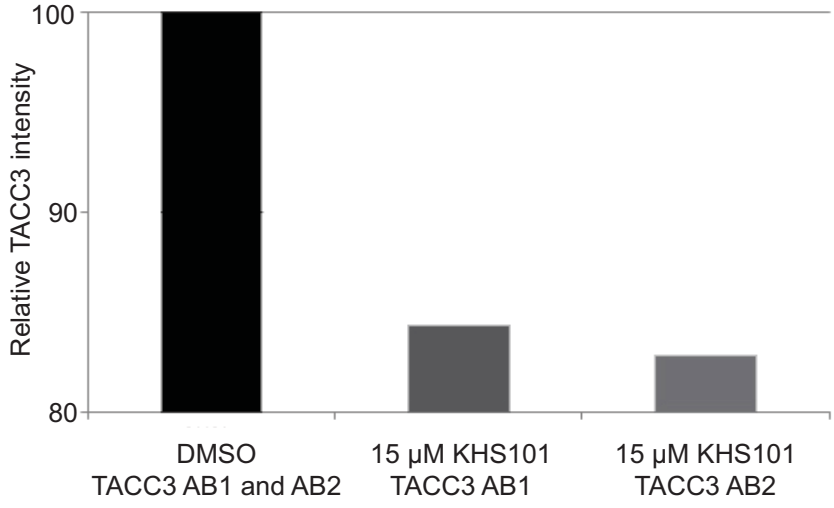

c.

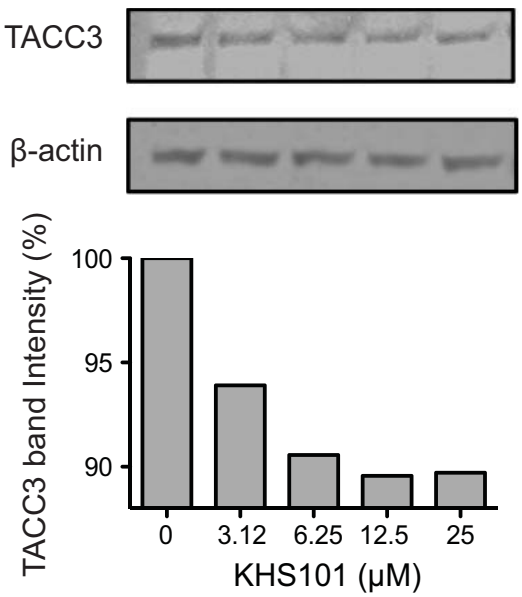

Guo et al
Supporting Figure 9